frontiers | Frontiers in Physics

TYPE Original Research
PUBLISHED 09 September 2022
DOI 10.3389/fphy.2022.1008784

OPEN ACCESS

EDITED BY
Santosh Kumar,
Liaocheng University, China

REVIEWED BY
Dharmendra Kumar,
Madan Mohan Malaviya University of Technology, India
Rahul Kumar Gangwar,
University of Delhi, India

*CORRESPONDENCE
Wei Li,
Liw@njupt.edu.cn

SPECIALTY SECTION
This article was submitted to Optics and Photonics,
a section of the journal
Frontiers in Physics

RECEIVED 01 August 2022
ACCEPTED 22 August 2022
PUBLISHED 09 September 2022

CITATION
Zhang Q, Li W, Ren Q, Zheng J, Xie Q and Wang X (2022), A D-type dual side-polished, highly sensitive, plasma refractive index sensor based on photonic crystal fiber.
Front. Phys. 10:1008784.
doi: 10.3389/fphy.2022.1008784

A D-type dual side-polished, highly sensitive, plasma refractive index sensor based on photonic crystal fiber

Qinrong Zhang[1,2], Wei Li[1,2]*, Qingyin Ren[1,2], Jiajin Zheng[1,2], Qiyun Xie[1,2] and Xiangfu Wang[1,2]

[1]College of Electronic and Optical Engineering and College of Flexible Electronics (Future Technology), Nanjing University of Posts and Telecommunications, Nanjing, China, [2]Jiangsu Province Engineering Research Center for Fabrication and Application of Special Optical Fiber Materials and Devices, Nanjing, China

In this paper, a D-shape dual side-polished (DSP) photonic crystal fiber (PCF) sensor based on high sensitivity and high range refractive index (RI) is proposed and analyzed. The surface of the structure is plated with Au and TiO_2, which can enhance the surface plasmon resonance (SPR) effect and sensitivity. The characteristics of the sensor were analyzed by finite element method (FEM). Its RI scope of detection is 1.38–1.42, and by optimizing geometric parameters, the optimal wavelength sensitivity (WS) is 22,100 nm/RIU. Additionally, the WS for DSP-PCF is far better than the recently reported PCF sensors in the above mentioned RI detection range to the best of our knowledge. With these significant outcomes over the analyte RI range, which is helpful for the fields of environmental detection and medical diagnosis.

KEYWORDS

surface plasmon resonance, photonic crystal fiber, wavelength sensitivity, refractive index, TiO2

Introduction

In recent years, photonic crystal fiber (PCF) have been widely used in medical diagnosis [1–4], temperature sensing [5, 6], environmental detection and other fields [7]. Various PCF structures have been discovered, such as D-shape structures [8], hexagonal inner metal coatings [9], multi-channel sensing structures [10], and outer metal coatings [11]. These structures can be roughly divided into two categories. In internal sensing, the pores of the PCF are selectively filled with analytes, while in external sensing the analytes are deposited on the surface of the sensor. So the feasibility of external sensing is higher. According to recent reports, the analyte medium and gold nano-ribbons are placed on the fiber surface, acting as external sensors, creating bidirectional channels, increasing sensitivity, and reducing surface coating area [12].

It has been reported that the selection of suitable PCF materials results in significantly enhanced coupling strength and sensitivity of the sensor. The most common plasma metals are gold and silver, respectively. Silver has sharper resonance peaks but is not

TABLE 1 Performance comparison of the proposed sensor with other recent reported PCF sensors.

Ref	year	Structure	RI range	Max sensitivity (nm/RIU)
[38]	2015	Ring based hexagonal PCF sensor	1.33–1.37	4,000
[39]	2016	Rectangular lattice and dual-core	1.33–1.41	14,216
[31]	2018	D-shaped and two micro-openings	1.31–1.37	11,750
[40]	2020	Ag–TiO_2 PCF-SPR	1.33–1.36	10,600
[41]	2020	Ag-ZnO coated D-PCF	1.37–1.40	6,000
[42]	2021	Side-polished PCF	1.35–1.39	12,500
This work	—	D-shape double-sided polished PCF-SPR sensor	1.38–1.42	22,100

chemically stable. Gold has a more pronounced resonance peak shift than silver. Gold is also less sensitive to temperature and humid issues than silver [13]. So, most of the PCF-SPR sensors have been conducted with gold as plasmonic metal. Moutusi De et al. proposed an efficient, birefringent D-shape PCF-SPR sensor using gold as the plasmonic metal with WS of 9,245 nm/RIU [14]. Depositing a layer of modifier material on the metal film can enhance the performance of the SPR sensor, TiO_2 has higher corrosion resistance and it can enable better interaction of surface plasmon with the attached metal layer [15, 16]. Emranul Haque et al. deposited TiO_2 on a metal film. They proposed a high-sensitivity SPR sensor based on a dual-core PCF with a maximum wavelength sensitivity (WS) of 10,600 nm/RIU [17]. The wavelength sensitivity is defined as a shift in resonance wavelength with respective to refractive index variation and follows the expression (d_L/d_n). In addition, by optimizing the size and arrangement of air holes in the PCF, the evanescent field strength can be increased to further enhance the property of the sensor. Haque E et al. [18] proposed a PCF based on D-shape square lattice pores, and the sensor has a WS of 20,000 nm/RIU. Jianfei Liao et al. [19] proposed a high-sensitivity near-infrared birefringent PCF sensor, which is a hexagonal internal sensing structure with an average sensitivity of 8,083 nm/RIU.

So far, our group has studied single-mode fibers based on cylindrical tapered [20] and cylindrical multi-mode fibers based on Au/ZnO/WS_2 [21]. In this paper, high-sensitivity D-type double-sided polished PCF-SPR sensor is proposed. Compared with single-mode fiber and multi-mode fiber, PCF has lower optical loss, higher optical non-linearity and can be modified by micro-structure design. Gold is selected as the plasmonic material for the sensor, and TiO_2 is deposited on the gold layer. TiO_2 can improve the coupling result between the core mode and the surface plasmon polarization (SPP) mode [22], thereby further enhancing the resonance of the sensor. By optimizing the structural parameters of the sensor, the maximum WS of the sensor is 22,100 nm/RIU. Considering the manufacturing error and feasibility, the sensor is optimized while analyzing the influence of changes in various parameters.

Geometry structure and theoretical modeling

Figure 1 is a 2D cross-sectional view of the proposed D-shape dual side-polished (DSP) PCF-SPR sensor with high sensitivity. It consists of 12 air holes, of which the inner air holes are arranged in a regular hexagonal structure, and the distance between adjacent air holes in the PCF is Λ. The diameter of the 6 small air holes in the inner layer is d_1, and the diameter of the 6 air holes in the outer layer is d_2. Both sides of the D-shape PCF are ground and polished surfaces, and the ground and polished surfaces are coated with gold nano-films and TiO_2 films. In order to improve the calculation accuracy, a perfectly matched layer (PML) is added to the outer wall of the fiber. The substrate material of the sensor is SiO_2, and the refractive index (RI) of SiO_2 can be calculated by the Sellmeier equation [23]:

$$n_{SiO2}^2(\lambda) = 1 + \frac{0.6961663\lambda^2}{\lambda^2 - 0.0046791} + \frac{0.4079426\lambda^2}{\lambda^2 - 0.0135120} + \frac{0.8974794\lambda^2}{\lambda^2 - 97.9340025} \quad (1)$$

where λ represents the wavelength of the incident light in microns. The dielectric constant of gold is derived from the Drude model [24]:

$$\varepsilon_{Au} = \varepsilon_\infty - \frac{\omega_D^2}{\omega(\omega + j\gamma_D)} - \frac{\Delta\varepsilon\Omega_L^2}{(\omega^2 - \Omega_L^2) + j\Gamma_L\omega} \quad (2)$$

Where ε_∞ represents the dielectric constant value at high frequency is 5.9673, ω is the angular frequency, Υ_D is the damping frequency, $\Upsilon_D/2\pi$ = 15.92 THz, ω_D is the plasmon frequency, $\omega_D/2\pi$ = 2,113.6 THz, Ω_L = 650.07 THz, $\Gamma_L/2\pi$ = 104.86 THz. TiO_2 is the adhesive layers that has been used in this paper. It helps gold to have a strong attachment with silica as well as to boost up the sensing performance. The RI of TiO_2 is derived from the following equation [25]:

$$n_{Ti} = \sqrt{5.913 + \frac{2.441 \times 10^7}{(\lambda^2 - 0.803 \times 10^7)}} \quad (3)$$

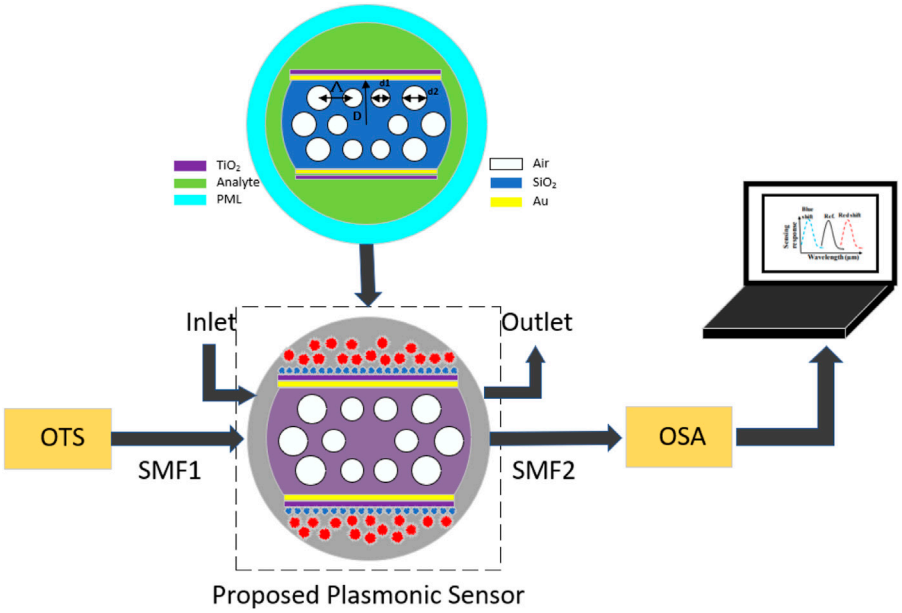

FIGURE 1
2D view of the schematic cross section and practical setup for the proposed DSP-PCF sensor.

The whole simulation has been employed in Comsol Multiphysics v5.5. The total sensor radius is kept at 6.7 μm with a non-physical PML employed at the outermost layer of the fiber having a thickness of 0.9 μm, which is around 13% of the total radius. PML acts like a boundary condition that absorbs surface radiations. The physical and optical properties of PML should be the same as the background material of the fiber to avoid noteworthy changes in sensing performance. However, fabricating the lattice design is manageable by utilizing the existing technologies. The sensor provides circular air holes of different sizes and is coated with gold and titanium dioxide. The Stack-and-draw technique potentially fabricates annular air holes [26]. Reference [27] established a fiber side-polishing system to achieve PCF polishing. In this polished system, the abrasive wheel can move back and forth in the horizontal direction during the polishing process and its lapping films can be easily replaced. Thus, we can control the horizontal moving range of the abrasive wheel to determine the side-polished length of the PCF. Compared with the fabrication of the D-shaped PCF in a curved V-groove [28], this technology can be used to control the side-polished length h and the SPL of the D-shaped PCF more accurately, which can meet the requirements of different designs. Chemical vapor deposition (CVD), wheel polishing, or high-pressure chemical deposition can be utilized for coating the thin layers of gold, TiO_2 [26].

Although the proposed sensor is theoretically designed, a schematic experimental setup of the sensor's sensing system in practice is shown in Figure 1. The system consists of an optically tunable source (OTS), polarization controller, and optical spectrum analyzer (OSA), connected by a single-mode fiber (SMF). The analyte is located on the outside of the PCF, and the inlet (the analyte) and the outlet (the analyte) are controlled by a pump. When the RI of the analyte changes, a blue or red shift of the loss peak can be observed.

Results and discussion

The sensing characteristics of the PCF were numerically simulated by the FEM software COMSOL Multiplicity with an an-isotropic perfectly matched layer. After optimizing the geometry parameters of PCF, take d_1 = 1 μm, d_2 = 1.4 μm, Λ = 1.89 μm, polishing depth D = 3 μm, gold film thickness t = 20 nm, TiO_2 thickness g = 10 nm. Figure 2 shows the dispersion correlation between the plasmon and the core mode when the refractive index is 1.39, in which the red curve is the spectral loss diagram of resonance, and the blue and green curves represent the effective refraction of the core mode and the SPP mode, respectively. In a photonic crystal fiber, air holes basically work as the cladding region. When light is transmitted, the whole optical field is confined within the core mode. On the contrary, SPP mode appears at the sensing medium where the plasmonic material has been coated. At the resonance condition, the wave vector of incident light of the core mode and surface plasmonic waves of the SPP mode gets equal with each other, which can also be defined as a phase-

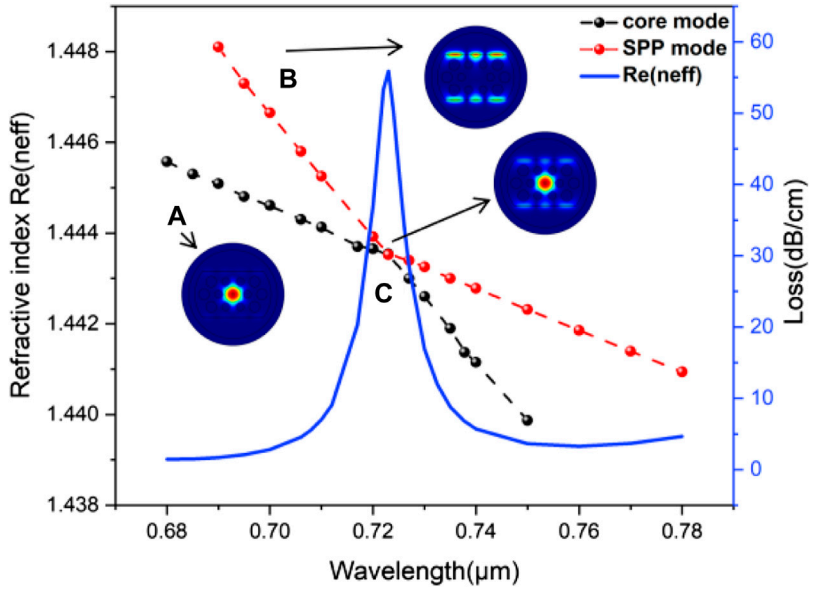

FIGURE 2
Dispersion relation of the core mode and the SPP mode and loss spectrum. Insets **(A–C)**: Energy distribution at each point.

matching condition [29]. Inset 1) shows the core mode of y-polarization, and almost all the energy is confined to the core. Inset 2) shows the SPP mode of y-polarization, and energy is penetrated on the Au-TiO_2 and analyte interface.

As resonance condition is satisfied, a loss peak is observed in narrow band that shows the wavelength shifts corresponding to any change in RI of sensing or dielectric medium adjacent to metal layer. In case of PCF SPR sensors, at resonance condition, as real part of effective RI of core mode matches with effective RI of surface plasmon mode, and maximum energy is exchanged from core mode to surface plasmon mode [12].

As can be seen from Figure 2, the real part of the effective refractive index of the core mode and the SPP mode both decrease with the increase of the wavelength, but the real part of the SPP mode decreases faster, and the loss also increases with the increase of the wavelength. The resonance occurs at 0.723 μm where the real part of effective index of the core guided mode and SPP mode cross each other and the imaginary part of the core mode is maximum. At this wavelength, the Re (n_{eff}) of the core mode and the SPP mode are equal, and the matching condition is satisfied, that is, the SPR effect occurs at the intersection of the two curves.

The propagation loss or confinement loss has been calculated by the following equation [30]:

$$\propto = \frac{40*\pi*Im\left(n_{eff}\right)}{ln\ (10)*\lambda} \approx 8.686 \times k_0*Im\left(n_{eff}\right) \times 10^4 \quad (4)$$

where, number of waves in free space is specified by, k0 = 2π/λ, operating wavelength is determined by λ and imaginary part of the effective RI is represented by Im (n_{eff}).

We can improve the performance of the sensor by optimizing the parameters of the sensor. The optimization process is to continuously adjust some parameters and keep the rest of the parameters unchanged. So far, many researchers [31–34] have adopted this approach. The parameters that need to be optimized are air hole diameters d_1 and d_2, gold film thickness *t*, TiO_2 thickness g, adjacent air hole spacing Λ, and polishing depth D.

The thickness of the gold film greatly affects the performance of the sensor. Thin gold layers lead to weak coupling between core and SPP modes, while thicker gold layers lead to over-coupling between core and SPP modes. Figure 3A shows the dependence of the loss spectrum on the change in Au film thickness t from 19 to 21 nm for the analyte RI of 1.41 and 1.42. It can be found that the resonance wavelength gradually red-shifts with the increase of the thickness of the Au film. According to Figure 3A, when the Au film thickness is 19 nm, 20 nm, 21 nm, the resonance loss peak shifts are 144, 167, and 206 nm, respectively. When the thickness is 21 nm, the offset is the largest, but there is no full width at half maximum of the resonance peak at this time. Therefore, the thickness of the Au film was chosen to be 20 nm. According to the relationship between thickness and sensitivity shown in the figure, in order to obtain a sensor with maximum performance, the manufacturing tolerance of Au film needs to be controlled within the upper and lower limits of 5%.

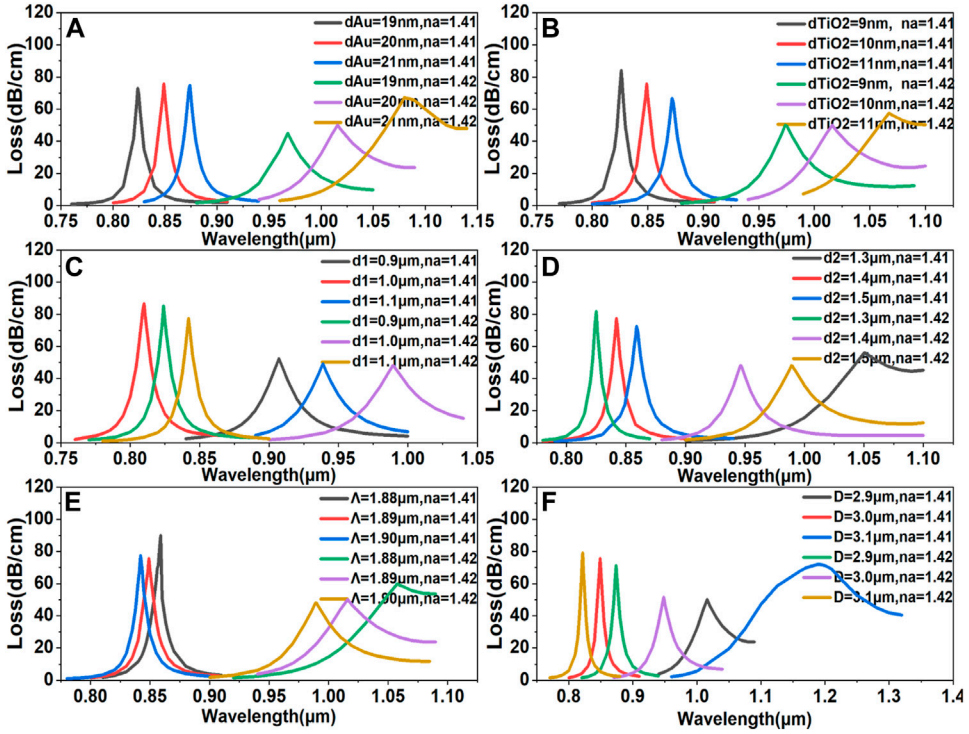

FIGURE 3
Confinement loss due to change in **(A)** gold thickness. **(B)** TiO_2 thickness. **(C)** Air pore diameter d_1. **(D)** Air pore diameter d_2. **(E)** Adjacent air hole spacing Λ. **(F)** Polishing depth D.

Figure 3B shows the correlation of the loss spectrum with the change in TiO_2 thickness g from 9 to 11 nm for analyte RI of 1.41 and 1.42. The TiO_2 layer has an effect on enhancing the evanescent field which can act as a transition metal and help to attract the evanescent field of the core [35], the interaction between the plasmon and the metal evanescent field will be enhanced, and the sensitivity will be increased. According to Figure 3B, the resonance wavelength is gradually red-shifted with the increase of TiO_2 thickness, and the resonance loss peak shifts are 148, 167, and 195 nm when the TiO_2 thickness is 9, 10, and 11 nm, respectively. Although the offset is the largest when the thickness is 11 nm, there is no full width at half maximum of the resonance peak. Therefore, the thickness of the TiO_2 film was chosen to be 10 nm. According to the relationship between thickness and sensitivity shown in the figure, in order to obtain a sensor with maximum performance, the manufacturing tolerance of TiO_2 film needs to be controlled within the upper and lower limits of 10%.

The structural parameters of the sensor are crucial to the performance of the sensor and have a significant impact on the resonant wavelength. Figure 3C shows the dependence of the loss spectrum on the variation of the air hole diameter d1 from 0.9 to 1.1 μm for RI of 1.41 and 1.42. It can be seen from the figure that when d_1 increases from 0.9 to 1.1 μm, the loss drops from 85.28 dB/cm to 66.39 dB/cm, so increasing d_1 will reduce the loss and the energy can be well confined to the core. Besides, the resonance wavelength gradually red-shifts with the increase of d_1, which indicates that the pore radius can tune the resonance intensity. And when d_1 is 0.9, 1, and 1.1 μm, the resonance loss peak shift amounts are 115, 147, and 208 nm, respectively. Since there is no full width at half maximum when d_1 = 1.1 μm, d_1 = 1 μm is the best choice for this design considering the offset and waveform. According to the relationship between thickness and sensitivity shown in the figure, in order to obtain a sensor with maximum performance, the manufacturing tolerance needs to be controlled within the upper and lower limits of 10%.

Figure 3D shows the dependence of the loss spectrum on the change in air pore diameter d_2 from 1.3 to 1.5 μm for analyte RI of 1.41 and 1.42. According to Figure 3D, the resonance loss keeps increasing as d_2 increases. This is because as the radius keeps increasing, it gradually squeezes the maximum light energy in the core region and helps the energy to couple with the SPP mode, so the loss will be high [30]. And when d_2 is 1.3, 1.4, and 1.5 μm, the resonance loss peak shift amounts are 192, 147, and 121 nm, respectively. Among them, when d_2 is 1.3 μm, the offset is the largest, but when d_2 is 1.3 μm, the full width at half maximum of the resonance peak does not exist, so the air hole diameter d_2 is selected to be 1.4 μm. According to the relationship between thickness and sensitivity shown in the

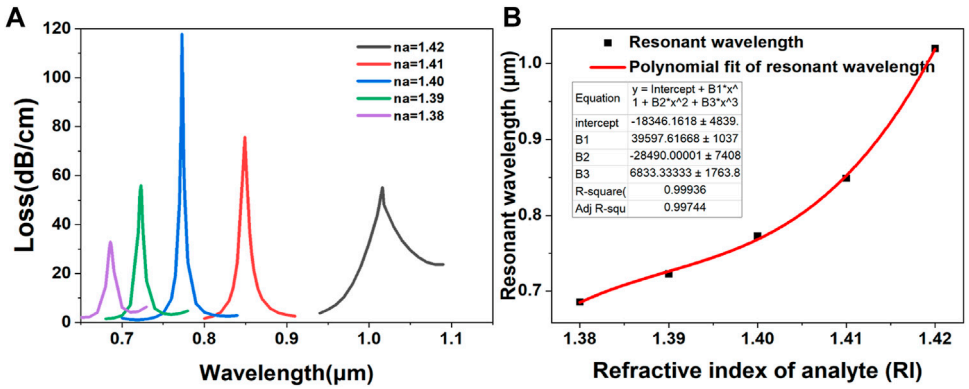

FIGURE 4
(A) Loss spectra of the proposed sensor along its full analyte RI detection range between 1.38 and 1.42. **(B)** Polynomial fitting curve with the RI variation from 1.38 to 1.42.

figure, in order to obtain a sensor with maximum performance, the manufacturing tolerance needs to be controlled within the upper and lower limits of 7%.

Figure 3E shows the dependence of the loss spectrum on the change in adjacent air hole spacing Λ from 1.88 to 1.90 μm for analyte RI of 1.41 and 1.42. It can be seen from the figure that the resonance wavelength is gradually blue-shifted with the increase of the adjacent air hole spacing Λ, because the interaction between the core mode and the SPP mode decreases when Λ increases [36]. And when Λ is 1.88, 1.89, and 1.90 μm, the resonance loss peak shift amounts are 167, 197, and 147 nm, respectively. Among them, when Λ is 1.89 μm, the offset is the largest, that is, when Λ is 1.89 μm, the wavelength sensitivity is the highest, and when Λ is 1.89 μm, the loss is the smallest. Therefore, the distance between adjacent air holes is selected to be 1.89 μm. According to the relationship between thickness and sensitivity shown in the figure, in order to obtain a sensor with maximum performance, the manufacturing tolerance needs to be controlled within the upper and lower limits of 0.5%.

Figure 3F shows the dependence of the loss spectrum on the change in polishing depth D from 2.9 to 3.1 μm for analyte RI of 1.41 and 1.42. According to Figure 3F, the loss gradually decreases as the polishing depth D increases. This is caused by the weak coupling between the core mode and the SPP mode, on the contrary, the loss will gradually increase with the decrease of the polishing depth. This is because the channel between the core and the metal surface is relatively small, and the small channel supports better coupling [37]. And when the polishing depth D is 2.9, 3, and 3.1 μm, the resonance loss peak shift amounts are 126, 167, and 316 nm, respectively. Among them, when D is 3.1 μm, the offset is the largest, but when D is 3.1 μm, the full width at half maximum of the resonance peak does not exist, so the polishing depth D is selected to be 3 μm. The loss spectrum varies greatly when D = 3.1 μm and RI is 1.42, because relatively more light leakage occurs at the core as the distance from the core to the surface increases. This results in insufficient core mode strength, so that relatively high losses occur in the coupling of the core mode to the plasmon mode of the metal surface [38]. According to the relationship between thickness and sensitivity shown in the figure, in order to obtain a sensor with maximum performance, the manufacturing tolerance needs to be controlled within the upper and lower limits of 3%.

Figure 4A shows the loss curves at different analyte RI (ranging from 1.38 to 1.42). It can be seen from the figure that with the increase of RI, the resonance wavelength is gradually red-shifted, which is because the coupling between the core mode and the SPP mode is continuously enhanced. And the loss first increases and then decreases with the increase of RI, and reaches a peak when RI is 1.4. Figure 4B is the fitted curve of the resonance wavelength as a function of analyte RI. The fitting coefficient R^2 is 0.99936. As can be seen from the figure, when the analyte RI is 1.42, the wavelength sensitivity reaches a maximum of 22,100 nm/RIU.

Conclusion

In order to clearly show the superiority of the designed symmetrically polished D-shaped RI sensor based on Au-TiO_2, it is compared with some sensors reported in recent years in terms of performance parameters as shown in Table 1. In this paper, a high-sensitivity D-shape double-sided polished PCF-SPR sensor based on Au-TiO_2 is proposed. And based on the finite element method, the RI sensing characteristics are numerically analyzed. The results show a maximum wavelength sensitivity of 22,100 nm/RIU in the refractive index range of 1.38–1.42. Because the designed D-type sensor has a simple structure and adopts an external sensing method, it has potential application prospects in the fields of biology and medicine.

Data availability statement

The original contributions presented in the study are included in the article/supplementary material, further inquiries can be directed to the corresponding author.

Author contributions

QZ: Writing—review and editing. WL: Writing—original draft, supervision, project administration, writing review and editing. QR: Writing—review and editing. JZ: Writing—review and editing. QX: Writing—review and editing. XW: Writing—original draft. All authors have read and agreed to the published version of the manuscript.

Funding

This work was supported by Natural Science Research Projects of Jiangsu Province University (20KJA510001), and middle-aged academic leader of Qing Lan Project in Jiangsu universities.

Conflict of interest

The authors declare that the research was conducted in the absence of any commercial or financial relationships that could be construed as a potential conflict of interest.

Publisher's note

All claims expressed in this article are solely those of the authors and do not necessarily represent those of their affiliated organizations, or those of the publisher, the editors and the reviewers. Any product that may be evaluated in this article, or claim that may be made by its manufacturer, is not guaranteed or endorsed by the publisher.

References

1. Krohn DA, MacDougall T, Mendez A. *Fiber optic sensors: Fundamentals and applications*. Bellingham, WA: Spie Press (2014). p. 233–310.

2. Poli F, Cucinotta A, Selleri S. *Photonic crystal fibers: Properties and applications*. Berlin, Germany: Springer Science & Business Media (2007). Vol. 102.

3. Rifat AA, Ahmed R, Yetisen AK, Butt H, Sabouri A, Mahdiraji GA, et al. Photonic crystal fiber based plasmonic sensors. *Sensors Actuators B: Chem* (2017) 243:311–25. doi:10.1016/j.snb.2016.11.113

4. Rindorf L, Jensen JB, Dufva M, Pedersen LH, Hoiby PE, Bang O. Photonic crystal fiber long-period gratings for biochemical sensing. *Opt Express* (2006) 14(18):8224–31. doi:10.1364/oe.14.008224

5. Weng S, Pei L, Wang J, Ning T, Li J. High sensitivity D-shaped hole fiber temperature sensor based on surface plasmon resonance with liquid filling. *Photon Res* (2017) 5(2):103–7. doi:10.1364/prj.5.000103

6. Mollah MA, Islam S, Yousufali M, Abdulrazak LF, Hossain MB, Amiri I. Plasmonic temperature sensor using D-shaped photonic crystal fiber. *Results Phys* (2020) 16:102966. doi:10.1016/j.rinp.2020.102966

7. Chakma S, Khalek MA, Paul BK, Ahmed K, Hasan MR, Bahar AN. Gold-coated photonic crystal fiber biosensor based on surface plasmon resonance: Design and analysis. *Sensing bio-sensing Res* (2018) 18:7–12. doi:10.1016/j.sbsr.2018.02.003

8. Romeiro AF, Cardoso MP, Silva AO, Costa JCWA, Giraldi MTR, Santos JL, et al. Multiparameter plasmonic resonance sensor using a D-shaped photonic crystal fiber. In: 2021 SBMO/IEEE MTT-S International Microwave and Optoelectronics Conference (IMOC). Fortaleza, Brazil: IEEE (2021). p. 1–4. doi:10.1109/IMOC53012.2021.9624780

9. Li D, Zhang W, Liu H, Hu J, Zhou G. High sensitivity refractive index sensor based on multicoating photonic crystal fiber with surface plasmon resonance at near-infrared wavelength. *IEEE Photon J* (2017) 9(2):1–8. doi:10.1109/jphot.2017.2687121

10. Liu C, Wang J, Jin X, Wang F, Yang L, Lv J, et al. Near-infrared surface plasmon resonance sensor based on photonic crystal fiber with big open rings. *Optik* (2020) 207:164466. doi:10.1016/j.ijleo.2020.164466

11. Paul AK, Hassan MZ, Islam MR, Zhu JG Graphene/gold based photonic crystal fiber plasmonic temperature sensor for electric vehicle applications. In: 2019 22nd International Conference on Electrical Machines and Systems (ICEMS). Harbin, China: IEEE (2019). p. 1–4.

12. Kaur B, Kumar S, Kaushik BK. (INVITED) advances in photonic crystal fiber: Sensing and supercontinuum generation applications. *Opt Fiber Technol* (2022) 72: 102982. doi:10.1016/j.yofte.2022.102982

13. Hao CJ, Lu Y, Wang MT, Wu BQ, Duan LC, Yao JQ. Surface plasmon resonance refractive index sensor based on active photonic crystal fiber. *IEEE Photon J* (2013) 5(6):4801108. doi:10.1109/jphot.2013.2292302

14. De M, Singh VK. Wide range refractive index sensor using a birefringent optical fiber. *Opt Quan Electron* (2021) 53(4):198–16. doi:10.1007/s11082-021-02847-6

15. Mahfuz AM, Hossain MA, Haque E, Hai NH, Namihira Y, Ahmed F. Dual-core photonic crystal fiber-based plasmonic RI sensor in the visible to near-IR operating band. *IEEE Sens J* (2020) 20(14):7692–700. doi:10.1109/jsen.2020.2980327

16. Islam MS, Cordeiro CMB, Sultana J, Aoni RA, Feng S, Ahmed R, et al. A Hi-Bi ultra-sensitive surface plasmon resonance fiber sensor. *IEEE access* (2019) 7: 79085–94. doi:10.1109/access.2019.2922663

17. Haque E, Mahmuda S, Hossain MA, Hai NH, Namihira Y, Ahmed F. Highly sensitive dual-core PCF based plasmonic refractive index sensor for low refractive index detection. *IEEE Photon J* (2019) 11(5):1–9. doi:10.1109/jphot.2019.2931713

18. Haque E, Hossain MA, Ahmed F, Namihira Y. Surface plasmon resonance sensor based on modified *D* -shaped photonic crystal fiber for wider range of refractive index detection. *IEEE Sens J* (2018) 18(20):8287–93. doi:10.1109/jsen.2018.2865514

19. Zhang S, Li J, Li S, Liu Q, Wu J, Guo Y. Surface plasmon resonance sensor based on D-shaped photonic crystal fiber with two micro-openings. *J Phys D Appl Phys* (2018) 51(30):305104. doi:10.1088/1361-6463/aace72

20. Wang D, Li W, Zhang Q, Liang B, Peng Z, Xu J, et al. High-performance tapered fiber surface plasmon resonance sensor based on the graphene/Ag/TiO2 layer. *Plasmonics* (2021) 16(6):2291–303. doi:10.1007/s11468-021-01483-w

21. Cai Y, Li W, Feng Y, Zhao JS, Bai G, Xu J, et al. Sensitivity enhancement of WS2-coated SPR-based optical fiber biosensor for detecting glucose concentration. *Chin Phys B* (2020) 29(11):110701. doi:10.1088/1674-1056/aba601

22. Haque E, Hossain MA, Namihira Y, Ahmed F. Microchannel-based plasmonic refractive index sensor for low refractive index detection. *Appl Opt* (2019) 58(6):1547–54. doi:10.1364/ao.58.001547

23. Malitson IH. Interspecimen comparison of the refractive index of fused silica. *J Opt Soc Am* (1965) 55(10):1205–9. doi:10.1364/josa.55.001205

24. Vial A, Grimault AS, Macías D, Barchiesi D, de la Chapelle ML. Improved analytical fit of gold dispersion: Application to the modeling of extinction spectra with a finite-difference time-domain method. *Phys Rev B* (2005) 71(8):085416. doi:10.1103/physrevb.71.085416

25. DeVore JR. Refractive indices of rutile and sphalerite. *J Opt Soc Am* (1951) 41(6):416–9. doi:10.1364/josa.41.000416

26. Paul AK, Sarkar AK, Rahman ABS, Khaleque A. Twin core photonic crystal fiber plasmonic refractive index sensor. *IEEE Sens J* (2018) 18(14):5761–9. doi:10.1109/jsen.2018.2841035

27. Chen Y, Xie Q, Li X, Zhou H, Hong X, Geng Y. Experimental realization of D-shaped photonic crystal fiber SPR sensor. *J Phys D Appl Phys* (2016) 50(2):025101. doi:10.1088/1361-6463/50/2/025101

28. Kim HJ, Kwon OJ, Han YG, Lee MK, Lee SB. Surface long-period fiber gratings inscribed in photonic crystal fibers. *J Korean Phys Soc* (2010) 57:1956–9. doi:10.3938/jkps.57.1956

29. Haque E, Al Noman A, Hossain MA, Hai NH, Namihira Y, Ahmed F. Highly sensitive D-shaped plasmonic refractive index sensor for a broad range of refractive index detection. *IEEE Photon J* (2021) 13(1):1–11. doi:10.1109/jphot.2021.3055234

30. Rifat AA, Ahmed R, Mahdiraji GA, Adikan FRM. Highly sensitive D-shaped photonic crystal fiber-based plasmonic biosensor in visible to near-IR. *IEEE Sens J* (2017) 17(9):2776–83. doi:10.1109/jsen.2017.2677473

31. Haider F, Aoni RA, Ahmed R, Islam MS, Miroshnichenko AE. Propagation controlled photonic crystal fiber-based plasmonic sensor via scaled-down approach. *IEEE Sens J* (2018) 19(3):962–9. doi:10.1109/jsen.2018.2880161

32. Falah AAS, Wong WR, Adikan FRM. Single-mode eccentric-core D-shaped photonic crystal fiber surface plasmon resonance sensor. *Opt Laser Technol* (2022) 145:107474. doi:10.1016/j.optlastec.2021.107474

33. Yang Y, Qin Y, Lu X, Zeng Y. High-sensitivity three-core photonic crystal fiber sensor based on surface plasmon resonance with gold film coatings. *Jpn J Appl Phys* (2021) 60(12):122002. doi:10.35848/1347-4065/ac2e68

34. Liu Y, Chen H, Guo Y, Wang M, Meng X, Jing X, et al. Ultra-high sensitivity plasmonic sensor based on D-shaped photonic crystal fiber with offset-core. *Optik* (2020) 221:165309. doi:10.1016/j.ijleo.2020.165309

35. Gao D, Guan C, Wen Y, Zhong X, Yuan L Multi-hole fiber based surface plasmon resonance sensor operated at near-infrared wavelengths. *Opt Commun* (2014) 313:94–8. doi:10.1016/j.optcom.2013.10.015

36. Islam MS, Sultana J, Aoni RA, Habib MS, Dinovitser A, Ng BWH, et al. Localized surface plasmon resonance biosensor: An improved technique for SERS response intensification. *Opt Lett* (2019) 44(5):1134–7. doi:10.1364/ol.44.001134

37. Wang Y, Li S, Wang M, Yu P. Refractive index sensing and filtering characteristics of side-polished and gold-coated photonic crystal fiber with a offset core. *Opt Laser Technol* (2021) 136:106759. doi:10.1016/j.optlastec.2020.106759

38. Rifat AA, Mahdiraji GA, Chow DM, Shee Y, Ahmed R, Adikan F. Photonic crystal fiber-based surface plasmon resonance sensor with selective analyte channels and graphene-silver deposited core. *Sensors* (2015) 15(5):11499–510. doi:10.3390/s150511499

39. An G, Li S, Yan X, Zhang X, Yuan Z, Zhang Y. High-sensitivity and tunable refractive index sensor based on dual-core photonic crystal fiber. *J Opt Soc Am B* (2016) 33(7):1330–4. doi:10.1364/josab.33.001330

40. Fang H, Wei C, Wang D, Yuan L, Jiao S, Bao Z, et al. Research on photonic crystal fiber based on a surface plasmon resonance sensor with segmented silver-titanium dioxide film. *J Opt Soc Am B* (2020) 37(3):736–44. doi:10.1364/josab.373395

41. Liang H, Shen T, Feng Y, Liu H, Han W. A D-shaped photonic crystal fiber refractive index sensor coated with graphene and zinc oxide. *Sensors* (2020) 21(1):71. doi:10.3390/s21010071

42. Haider F, Aoni RA, Ahmed R, Jen Chew W, Amouzad Mahdiraji G. Plasmonic micro-channel based highly sensitive biosensor in visible to mid-IR. *Opt Laser Technol* (2021) 140:107020. doi:10.1016/j.optlastec.2021.107020